J. Fluid Mech. (2006), *vol.* 558, *pp.* 79–102.
doi:10.1017/S002211200600989X Printed in the United Kingdom

Wall pressure fluctuations and flow-induced noise in a turbulent boundary layer over a bump

By JOONGNYON KIM AND HYUNG JIN SUNG†

Department of Mechanical Engineering, Korea Advanced Institute of Science and Technology, 373-1 Guseong-dong, Yuseong-gu, Daejeon, 305-701, Korea

(Received 18 February 2005 and in revised form 28 November 2005)

Direct numerical simulations of a turbulent boundary layer over a bump were performed to examine the effects of surface longitudinal curvature on wall pressure fluctuations (p_w) and flow-induced noise. Turbulence statistics and frequency spectra were obtained to elucidate the response of wall pressure fluctuations to the longitudinal curvature and to the corresponding pressure gradient. Wall pressure fluctuations were significantly enhanced near the trailing edge of the bump, where the boundary layer was subjected to a strong adverse pressure gradient. Large-scale structures in the distribution of wall pressure fluctuations were observed to grow rapidly near the trailing edge of the bump and convect downstream. Acoustic sources of the Lighthill equations were investigated in detail at various longitudinal surface curvatures. The acoustic sources (S) were highest near the trailing edge of the bump, where the root mean square wall pressure fluctuations were greatest. The maximum correlation coefficient between p_w and S was located just above the location of maximum wall pressure fluctuations. Far-field acoustic density fluctuations were computed using the Lighthill acoustic analogy. We found that the surface dipole is dominant in the total acoustic field. The contribution of the volume quadrupoles to the total acoustic field gradually increases with increasing radius of the surface curvature (δ/R).

1. Introduction

The turbulent boundary layer of a flow passing over a bump exhibits extremely complex flow characteristics, despite the relatively simple geometry of this system. A model surface bump can be constructed from three tangential circular arcs, as shown in figure 1. When the flow impinges on this bump, the boundary layer experiences a short region of concave surface, a longer region of convex surface, another short region of concave surface, and then returns to the flat plate. As a result of this geometry, the streamwise pressure gradient changes from adverse to favourable in the region upstream of the bump apex. Downstream of the bump apex, the boundary layer is subjected to an adverse pressure gradient before returning to a favourable pressure gradient over the flat plate. Thus, if we are to design an effective strategy for controlling the noise generated by such flows, a clear understanding of the effect of the longitudinal surface curvature and the associated pressure gradient is essential. One practical example in which such knowledge is vital is noise generation caused by flow over sonar transducers mounted on ships or submarines.

† Author to whom correspondence should be addressed: hjsung@kaist.ac.kr.

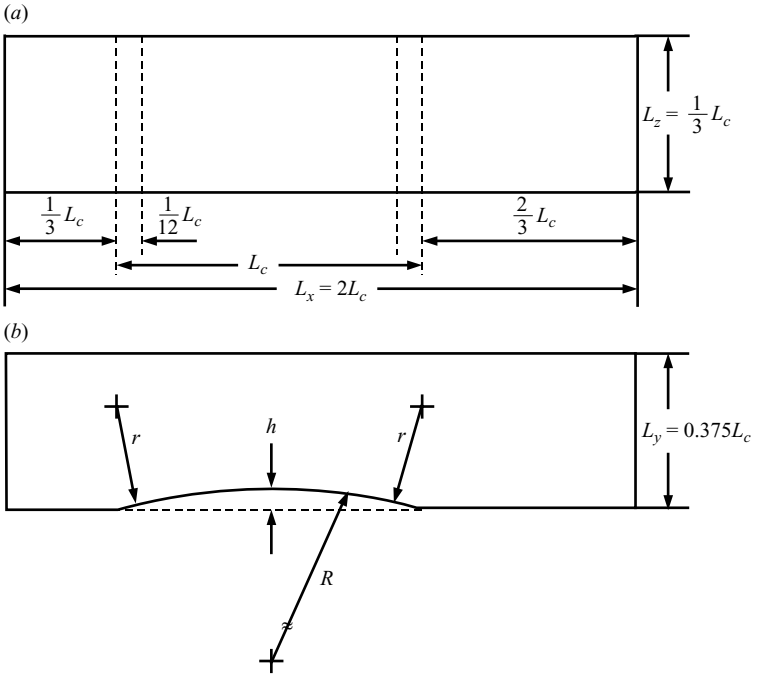

FIGURE 1. Schematic diagram of the flow geometry. (*a*) Top view of the computational domain; (*b*) side view of the computational domain.

A response to perturbations in both surface curvature and pressure gradient has been the subject of several investigations (Baskaran, Smits & Joubert 1987; Webster DeGraaff & Eaton 1996; Wu & Squires 1998). It is known that an internal layer is triggered by the discontinuity in longitudinal surface curvature. The internal layer is shown by knee points in the profiles of turbulence intensity. Baskaran *et al.* (1987) observed the formation of an internal layer at the discontinuity in the surface curvature and the subsequent growth of this layer over the convex surface. The streamwise turbulence intensity is significantly increased in the internal layer rather than in the outer layer. Most of the flow behaviour and internal layer could be accounted for in terms of pressure gradient effects (Webster *et al.* 1996). Wu & Squires (1998) suggested that the abrupt increase of skin friction caused by the presence of a pressure gradient enhances near-wall turbulence stresses and plays a key role in the formation of the internal layer.

Wall pressure fluctuations, which are directly related to the surface excitation force, are associated with flow unsteadiness and noise generation in the immediate vicinity of the wall. A knowledge of these quantities is of prime importance in understanding the dynamic behaviour of wall turbulent flow. The majority of previous studies on wall pressure fluctuations have focused on the equilibrium turbulent boundary layers over flat plates or inside channels (Kim, 1989; Choi & Moin 1990; Kim, Choi & Sung 2002). Recent advances in direct numerical simulation (DNS) have intensified interest in calculating wall pressure fluctuations in non-equilibrium turbulent flows. Neves & Moin (1994) examined the effects of convex transverse curvature on wall pressure fluctuations in axial-flow boundary layers. They found that root mean square (r.m.s.) wall pressure fluctuations decrease with increasing transverse curvature. In a

study of the effects of separation on wall pressure fluctuations, Na & Moin (1998) observed large two-dimensional roller-type structures inside a separation bubble. Kim, Kim & Sung (2003) investigated the characteristics of wall pressure fluctuations after a sudden application of wall blowing or suction. They showed that blowing has a greater effect than suction on wall pressure fluctuations. However, the effects of longitudinal surface curvature and the associated pressure gradient on wall pressure fluctuations have yet to be established.

The mechanism of aerodynamic noise generation by a turbulent shear flow has been a subject of great interest since Lighthill first formulated a general theory for the aeroacoustic noise (Lighthill 1952). When a flow encounters a solid body, Curle's integral solution (1955) to the Lighthill equation provides a theoretical framework for predicting the noise generated by the flow–body interaction. According to the extension of Lighthill's formalism by Powell (1960), fluctuating velocities produce quadrupole noise sources, whereas fluctuating wall shear stresses take the form of dipole sources. Thus, when an infinite surface plate boundary layer is assumed, the most important dipole source term, that from wall pressure fluctuations, is eliminated by reflection from the surface plate. However, in the present study, we found that the acoustic sources of the Lighthill equations without consideration of wall pressure fluctuations where closely correlated with the distribution of wall pressure fluctuations. Here we endeavour to develop a quantitative description of the relationship between wall pressure fluctuations and acoustic sources.

The main objective of the present study was to investigate the effects of longitudinal surface curvature and the associated pressure gradient on wall pressure fluctuations and flow-induced noise. To achieve this, we performed DNSs of a turbulent boundary layer over a bump. Turbulence statistics and frequency spectra of wall pressure fluctuations were extracted using standard techniques for analysing stochastic data. In addition, two-point correlation coefficients were used to deduce the spatial structure of the wall pressure fluctuations. Acoustic sources of the Lighthill equations were investigated in detail as a function of longitudinal surface curvature. A quantitative statistical description of the relationship between wall pressure fluctuations and acoustic sources was formulated in terms of the correlation coefficient. Far-field acoustic density fluctuations were computed using the Lighthill acoustic analogy.

2. Direct numerical simulation

For an incompressible flow, the non-dimensional governing equations are

$$\frac{\partial u_i}{\partial t} + \frac{\partial}{\partial x_j} u_i u_j = -\frac{\partial p}{\partial x_i} + \frac{1}{Re} \frac{\partial}{\partial x_j} \frac{\partial u_i}{\partial x_j}, \tag{1}$$

$$\frac{\partial u_i}{\partial x_i} = 0, \tag{2}$$

where x_i are the Cartesian coordinates and u_i are the corresponding velocity components. All variables are non-dimensionalized by a characteristic length and velocity scale, and Re is the Reynolds number.

By introducing generalized coordinates η^i, the velocity components u_i are transformed into the volume fluxes across the faces of the cell q^i or $\boldsymbol{q}$. Formulation of the problem in terms of the contravariant velocity components, weighted with the Jacobian J in conjunction with the staggered variable configuration, leads to

Case	δ/R	δ/h	R/L_c	r/L_c
1	0.015	3.0	4.64	0.92
2	0.030	1.5	2.32	0.46
3	0.045	1.0	1.56	0.31

TABLE 1. Comparison of bump parameters.

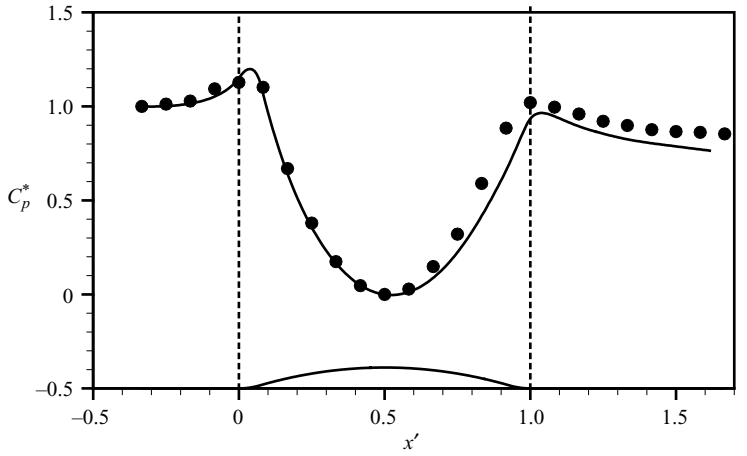

FIGURE 2. Comparison of —, calculated mean wall pressure with ●, the experimental data (Webster *et al.* 1996).

discretized equations. The transformed governing equations are rewritten as

$$\frac{\partial q^i}{\partial t} + N^i(q) = -G^i(p) + L_1^i(q) + L_2^i(q), \tag{3}$$

$$D^i q^i = \frac{1}{J}\left(\frac{\partial q^1}{\partial \eta^1} + \frac{\partial q^2}{\partial \eta^2}\right) + \frac{\partial q^3}{\partial \eta^3} = 0, \tag{4}$$

where N^i is the convective term, $G^i(p)$ is the pressure gradient term, L_1^i and L_2^i are the diffusion terms without and with cross-derivatives, and D^i is the divergence operator. More details can be found in Choi, Moin & Kim (1993). The governing equations are integrated in time using the fully implicit fractional-step method proposed by Choi & Moin (1994). The fractional step is a method of approximation of the governing equations based on the decomposition of the operators. In applying this method to the Navier–Stokes equations, we can interpret the role of pressure in the momentum equations as a projection operator, which projects an arbitrary vector field into a divergence-free vector. A second-order central difference scheme is used for the spatial derivatives and a Crank–Nicolson method is employed in time advancement. The discretized nonlinear momentum equations are solved by using a Newton iterative method. Solving the Poisson equation for p satisfies the continuity equation.

Table 1 gives the bump parameters used in the present work. In the present DNS, we specified the bump parameters so that the streamwise distribution of the computed wall pressure coefficient for $\delta/R = 0.015$ matched well with that of Webster *et al.* (1996) (figure 2). Here, δ is the boundary-layer thickness and R is the radius of convex curvature. Because the Reynolds number considered in the present DNSs

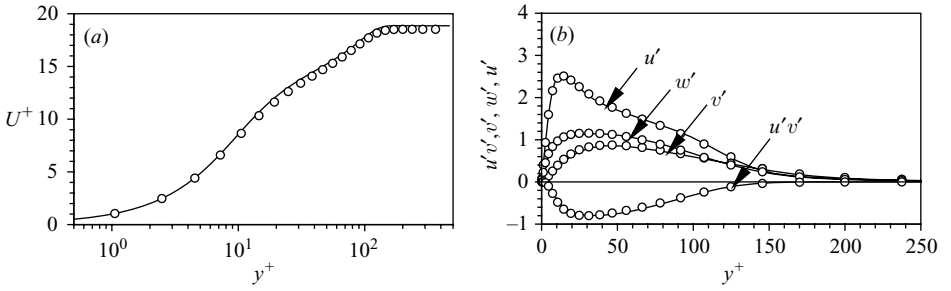

FIGURE 3. Comparison of turbulence statistics: (*a*) mean velocity profile; (*b*) turbulence intensities and Reynolds shear stress. —, present; ○, Spalart (1988).

was smaller than those of previous studies, a smaller curvature parameter (δ/R) was used in the present work. Bradshaw (1973) demonstrated that a convex curvature of $\delta/R = 0.01$ significantly reduced the skin friction coefficient compared to that over a flat plate. Taking into consideration this finding, the bump used in the present work is expected to affect the turbulent boundary layer significantly. The surface bump has two discontinuities in surface curvature: the concave-to-convex surface near the leading edge and the convex-to-concave surface near the trailing edge. Note that, at both of these discontinuities, the bump used in the present work has a value of $\Delta k^* = 5.52 \times 10^{-4}$, which satisfies the criterion $\Delta k^* > 0.37 \times 10^{-4}$ for the formation of an internal layer (Baskaran *et al.* 1987). Here, $\Delta k^* = (1/R_2 - 1/R_1)\nu/u_\tau$ where R_1 and R_2 are upstream and downstream radii of curvature, respectively.

In the DNSs, time-dependent turbulent inflow data were provided at the inlet based on the method of Lund, Wu & Squires (1998). Using this approach, instantaneous planes of velocity data were extracted from an auxiliary simulation of a spatially developing turbulent boundary layer over a flat plate. A plane velocity field near the domain exit was modified by the rescaling procedure and reintroduced to the inlet of the computational domain in the inflow-generation simulation. The main simulation of a turbulent boundary layer over a bump was then carried out. The convective boundary condition imposed at the exit had the form $(\partial u_i/\partial t) + c(\partial u_i/\partial x) = 0$, where c is the local bulk velocity. A no-slip boundary condition was imposed at the solid wall, and the boundary conditions on the top surface of the computational domain were $\partial u_1/\partial y = 0$, $u_2 = 0$ and $u_3 = 0$. Periodic boundary conditions were applied in the spanwise direction.

To ascertain the reliability and accuracy of the present numerical simulation, comparisons of the turbulence statistics with the DNS data of Spalart (1988) are made and presented in figure 3. The mean velocity profile normalized by the friction velocity is shown in figure 3(*a*), where $y^+ = yu_\tau/\nu$ and $U^+ = U/u_\tau$. Comparisons are extended to the turbulence intensities and Reynolds shear stress in figure 3(*b*). The present results are in excellent agreement with the DNS data at the same Reynolds number. This suggests that the resolution of the present study is sufficient to analyse the second-order turbulence statistics.

The computational domain size was $L_x = 240$, $L_y = 45$ and $L_z = 40$. The inlet Reynolds number based on the inlet momentum thickness (θ_0) and free-stream velocity (U_∞) was $Re = 300$. The mesh contained $257 \times 97 \times 129$ points in the streamwise, wall-normal, and spanwise directions, respectively. Non-uniform grid distributions were used in the streamwise and wall-normal directions, whereas a uniform grid distribution was used in the spanwise direction. The computational grid was generated

using the direct distribution control technique of Thomas & Middlecoff (1980). The computational time step used was $\Delta t = 0.3\,\theta_0/U_\infty$ and the total averaging time to obtain the statistics was $T_{avg} = 5000\,\nu/u_\tau^2$, where ν and u_τ are the kinematic viscosity and the friction velocity, respectively. A streamline-normal coordinate system (s, n, z) was used for post-processing, where the n-axis is perpendicular to the lower surface in figure 1(*b*). The corresponding velocity components in (s, n, z) are denoted by (u_s, u_n, u_z). A normalized streamwise coordinate, $x' = (x - x_0)/L_c$, was also used, where x_0 corresponds to the leading edge of the bump and L_c is the bump length. In the x'-coordinate system, $x' = 0$ coincides with the leading edge, $x' = 0.5$ with the bump apex and $x' = 1.0$ with the trailing edge.

3. Aeroacoustic theory

From the Lighthill acoustic analogy (1952), the concentrated unsteady flow region is the aeroacoustic source region, which can be obtained from an incompressible DNS. The density fluctuations due to propagation of an acoustic wave from the aeroacoustic source region are governed by an inhomogeneous wave equation, which can be written in the following form:

$$\frac{\partial^2 \rho}{\partial t^2} + \frac{1}{M^2}\frac{\partial^2 \rho}{\partial x_i \partial x_j} = \frac{\partial^2 T_{ij}}{\partial x_i \partial x_j}, \tag{5}$$

where

$$T_{ij} = \rho u_i' u_j' + \delta_{ij}(p - \rho/M^2) - \tau_{ij}, \tag{6}$$

$$\tau_{ij} = \frac{1}{Re}\left(\frac{\partial u_i'}{\partial x_j} + \frac{\partial u_j'}{\partial x_i} - \frac{2}{3}\delta_{ij}\frac{\partial u_k'}{\partial x_k}\right). \tag{7}$$

Equation (5) is a restatement of the Lighthill equation in terms of the values relative to the free-stream values. Equation (6) is the Lighthill stress tensor composed of three terms, and (7) is the viscous part of the Stokes stress tensor. All variables are non-dimensionalized by a characteristic length and velocity scale, and Re is the Reynolds number.

When the reference frame is fixed on the moving solid boundary, Curle's solution (1955) of the Lighthill acoustic analogy can be applied. Curle showed that the general solution for the flow past a rigid surface can be written as:

$$\rho(x,t) - 1 = \frac{M^2}{4\pi}\frac{\partial}{\partial x_i}\int_S n_j \frac{P_{ij}(y, t - Mr)}{r}\,\mathrm{d}^2 y + \frac{M^2}{4\pi}\frac{\partial^2}{\partial x_i \partial x_j}\int_V \frac{T_{ij}(y, t - Mr)}{r}\,\mathrm{d}^3 y, \tag{8}$$

where $\boldsymbol{x}$ is an observation point position vector, $\boldsymbol{y}$ is a source point position vector, $r = |\boldsymbol{x} - \boldsymbol{y}|$, $P_{ij} = p\delta_{ij} - \tau_{ij}$, and n_j is the directional cosine of the outward normal to the rigid surface.

Powell (1960) pointed out that for flow past an infinite plane surface, we can consider a new extended flow field obtained by reflection of the original one in the plane $y = 0$, which gives an identical acoustic field. Based on the result of Powell, the acoustic density in the upper half-plane can be written as:

$$\begin{aligned}\rho(x,t) - 1 = {} & \frac{M^2}{4\pi}\frac{\partial}{\partial x_k}\int_S \frac{\tau_{k2}(y, t - Mr)}{r}\,\mathrm{d}^2 y + \frac{M^2}{4\pi}\frac{\partial^2}{\partial x_i \partial x_j}\int_V \frac{T_{ij}(y, t - Mr)}{r}\,\mathrm{d}^3 y \\ & + \frac{M^2}{4\pi}\frac{\partial^2}{\partial x_i^* \partial x_j^*}\int_{V^*} \frac{T_{ij}(y, t - Mr^*)}{r^*}\,\mathrm{d}^3 y,\end{aligned} \tag{9}$$

where $k = 1, 3$ and $\boldsymbol{x}^*$ is the image of position $\boldsymbol{x}$ in the rigid surface $x_2 = 0$. Note that reflection at an infinite surface plate boundary layer thus eliminates the dipole source term arising from wall pressure fluctuations. When the distance between observation and source points is larger than the acoustic wavelength, the far-field approximation can be applied. Also, when the solid body and the source region are smaller than the typical acoustic wavelength, the source region is acoustically compact. The acoustic density at the far field generated from a compact source region can be approximated by

$$\rho(x,t) - 1 = \frac{M^3}{2\pi}\frac{x_k}{|x|^2}\frac{\partial}{\partial t}\int_S \tau_{k2}(y, t - Mr)\,\mathrm{d}^2 y + \frac{M^4}{4\pi}\frac{x_i x_j + x_i^* x_j^*}{|x|^3}\frac{\partial^2}{\partial t^2}\int_V T_{ij}(y, t - Mr)\,\mathrm{d}^3 y, \tag{10}$$

which includes two typical noise source functions, a surface dipole and a volume quadrupole, which are generated from the surface of the rigid wall and the entire unsteady flow region, respectively. The acoustic density at the far field generated by a compact source region is rewritten as:

$$\rho(x,t) - 1 = \frac{M^3}{2\pi}\frac{x_k}{|x|^2}\dot{D}_k(t - Mr) + \frac{M^4}{4\pi}\frac{x_i x_j + x_i^* x_j^*}{|x|^3}\ddot{Q}_{ij}(t - Mr), \tag{11}$$

where

$$\dot{D}_k(t - Mr) = \frac{\partial}{\partial t}\int_S \tau_{k2}(y,t)\,\mathrm{d}^2 y, \tag{12}$$

$$\ddot{Q}_{ij}(t - Mr) = \frac{\partial^2}{\partial t^2}\int_V T_{ij}(y,t)\,\mathrm{d}^3 y, \tag{13}$$

are dipole and quadrupole sources, respectively. The residual effect at the exit boundary is eliminated by using the following corrective formula derived by Wang, Lele & Moin (1996),

$$\ddot{Q}'_{ij} = \ddot{Q}_{ij} + \dot{F}_{ij}, \tag{14}$$

where the dots denote time derivatives and F_{ij} is the flux of Lighthill stress components (Wang *et al.* 1996).

4. Results and discussion

4.1. *Mean wall pressure and wall pressure fluctuations*

Before proceeding further, it would be advantageous to see the variation in the mean wall pressure along the wall. Figure 4(*a*) shows the streamwise distribution of the wall pressure coefficient (C_p). The boundary layer initially develops under a zero pressure gradient at the inlet, after which the streamwise pressure gradient becomes mildly adverse over the upstream flat plate. The boundary layer then experiences a short region of concave curvature before encountering a region of convex curvature. The corresponding pressure gradient changes from adverse to favourable. Downstream of the bump apex, the streamwise pressure gradient is strongly adverse then changes to mildly favourable over the exit flat plate.

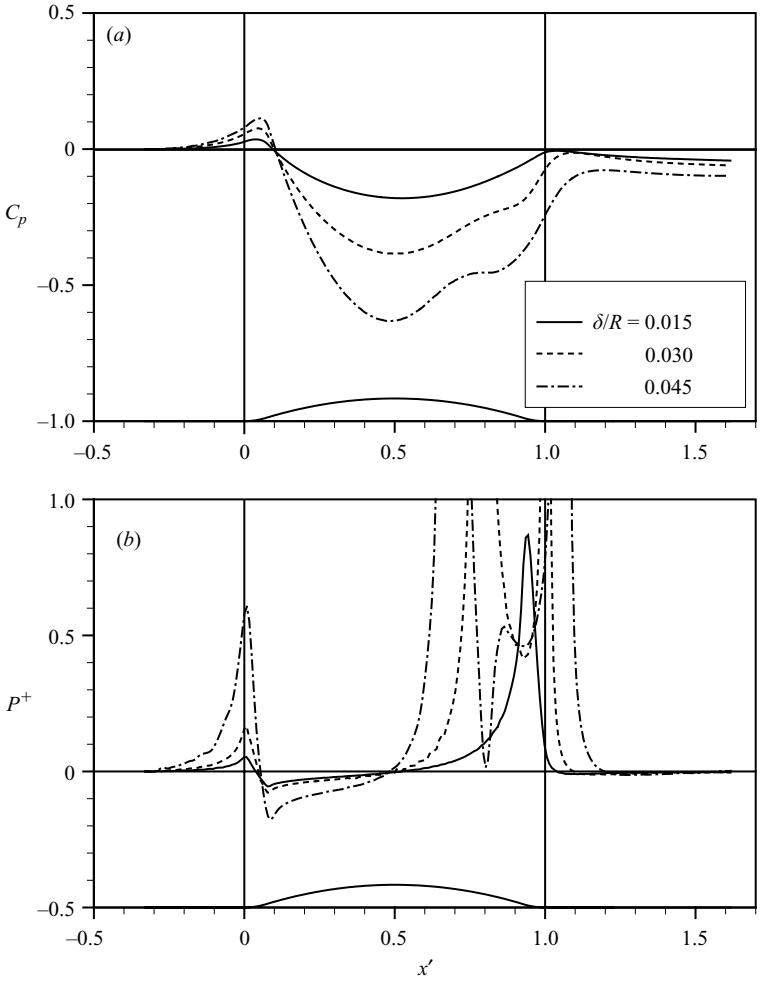

FIGURE 4. Streamwise distribution of (*a*) mean wall pressure coefficient and (*b*) pressure gradient parameter.

Figure 4(*b*) shows the distribution of the non-dimensional pressure gradient parameter P^+, which is given by

$$P^+ = \frac{\nu}{\rho u_\tau^3} \frac{\mathrm{d}\langle p_w \rangle}{\mathrm{d}s}. \tag{15}$$

Here u_τ is the friction velocity and the brackets indicate an average over the spanwise direction and time. For $\delta/R = 0.015$, P^+ changes sign at three streamwise locations, $x' = 0.038, 0.52$ and 1.04. Thus, the computational domain can be divided into four streamwise regions according to the sign of the streamwise pressure gradient. Notably, in the range of $0.78 < x' < 1.02$, P^+ exceeds the value of 0.09 suggested by Patel (1965) as the threshold value above which separation processes occur. In this region, which is the zone of strong adverse pressure gradient, the boundary layer experiences intermittent reversal and separation in the vicinity of the wall. This region of strong adverse pressure gradient expands with increasing δ/R.

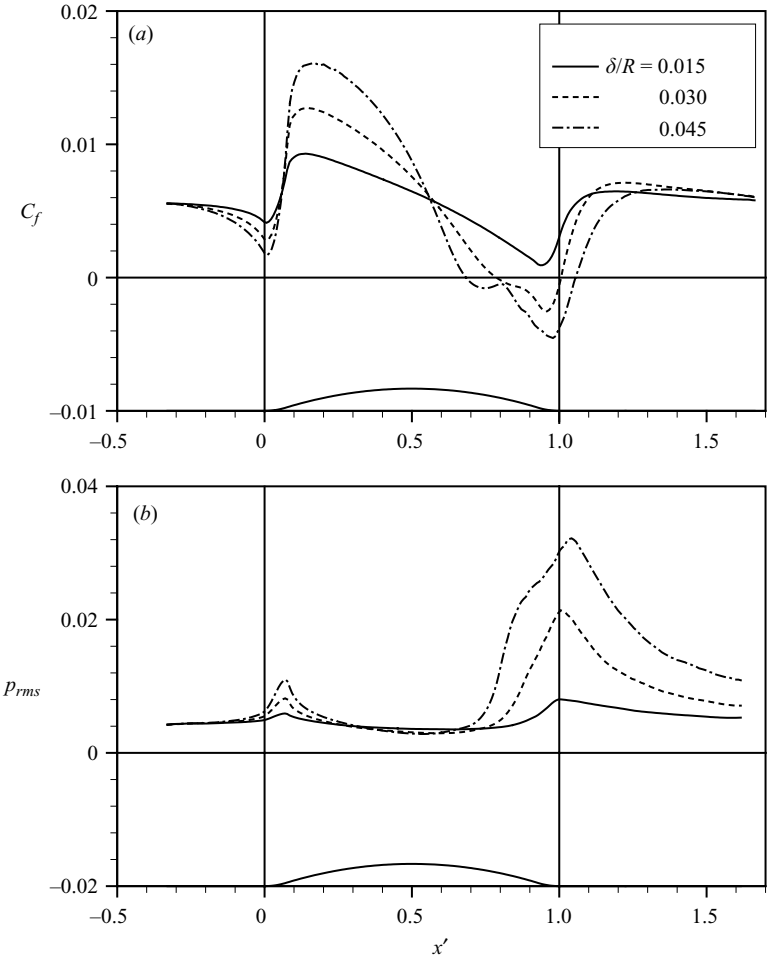

FIGURE 5. Streamwise distribution of (*a*) skin friction coefficient and (*b*) r.m.s. wall pressure fluctuations.

The distribution of the skin friction coefficient, $C_f = \tau_w/(\rho U_\infty^2/2)$, is shown in figure 5(*a*). Relative to C_f at the inlet, C_f decreases when the boundary layer is subjected to an adverse pressure gradient, but increases in regions of favourable pressure gradient. Near the flat-to-concave transition, C_f increases rapidly in the region where the pressure gradient decreases. A rapid increase in C_f also occurs near the trailing edge of the bump. As pointed out by Wu & Squires (1998), this latter change in C_f can be regarded as evidence of internal layer generation at a curvature discontinuity. The locations of zero wall shear stress are $x' = 0.78$ and $x' = 1.01$ for $\delta/R = 0.030$, and $x' = 0.68$ and $x' = 1.06$ for $\delta/R = 0.045$. Since detachment is related to the streaky structures from upstream of the bump apex, the location at which detachment occurs is more variable than that of reattachment.

The streamwise distributions of r.m.s. wall pressure fluctuations $(p_w)_{rms}$ normalized by the reference dynamic pressure $q_\infty = \rho U_\infty^2/2$ are displayed in figure 5(*b*). Two peaks are observed for all cases. The locations of these peaks, $x' = 0.07$ and $x' = 1.0$, approximately coincide with the concave-to-convex and concave-to-flat surface transitions, respectively. Over the downstream of the bump apex, $(p_w)_{rms}$ begins

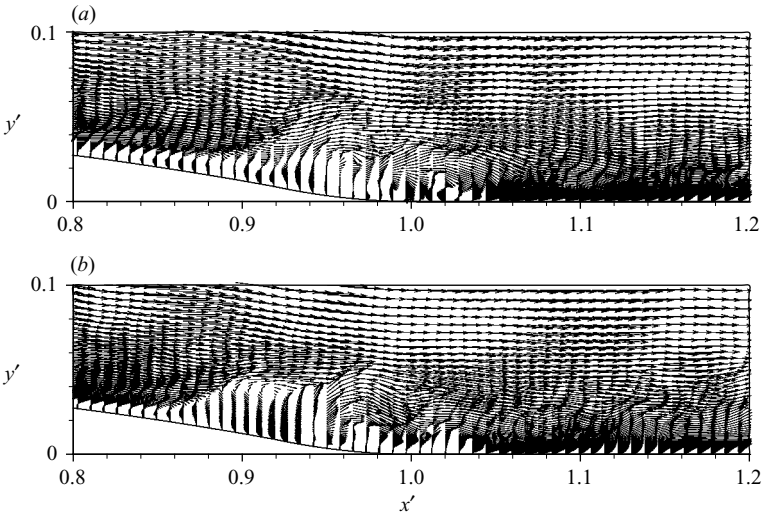

FIGURE 6. Side view of instantaneous velocity vectors in the (x, y)-plane for $\delta/R = 0.030$. (a) $tU_\infty/\theta_0 = 0$; (b) $tU_\infty/\theta_0 = 30$.

to increase near $x' = 0.8(\delta/R = 0.030)$ and $x' = 0.7(\delta/R = 0.045)$, where the pressure gradient parameter (P^+) exceeds the value of 0.09. Figure 6 shows instantaneous velocity vectors in the (x, y)-plane at the middle of the spanwise domain at two different instants. Comparison of the two velocity vector distributions shows that the instantaneous separation bubbles and associated shear layers change over time. The detachment and reattachment regions move up- and downstream, indicating the highly unsteady nature of the flow near the trailing edge of the bump.

Figure 7 shows contour maps of the instantaneous skin friction coefficient for surface curvatures of $\delta/R = 0.015$, 0.030 and 0.045. Solid and dotted lines denote positive and negative C_f, respectively. As the turbulent boundary layer moves through a region of adverse pressure gradient near the trailing edge of the bump, the flow decelerates until some reversal flow occurs. Close inspection of figure 7 reveals that the streaky structures disappear after the detachment region. The spanwise lines of detachment are related to the low-speed streaks that come from upstream of the bump. Small-scale structures are generated near the trailing edge of the bump and the low-speed streaks are completely destroyed.

To examine the spectral features of the wall pressure fluctuations, the frequency spectra of p_w are obtained using standard techniques for stochastic data. The wall pressure fluctuations $p_w(x, z, t)$ are Fourier-transformed in the spanwise direction and time. Letting $p_w(x, k_z, \omega)$ be the discrete Fourier transform of $p_w(x, z, t)$, the power spectral density is computed by

$$\Phi(k_z, \omega; x) = \langle \hat{p}_w(x, k_z, \omega)\hat{p}_w^*(x, k_z, \omega)\rangle, \tag{16}$$

where $*$ denotes the complex conjugate and the angle brackets indicate an average over the spanwise direction and time. The dependence of the spectral density on the streamwise location x is considered to be due to the flow inhomogeneity. The pressure spectra have been computed by using the ensemble average of the windowed part of the signal. The power spectral density $\Phi(k_z, \omega; x)$ is computed from the discrete Fourier transform of $p_w(x, z, t)$. The frequency spectra $\varphi(\omega; x)$ are obtained

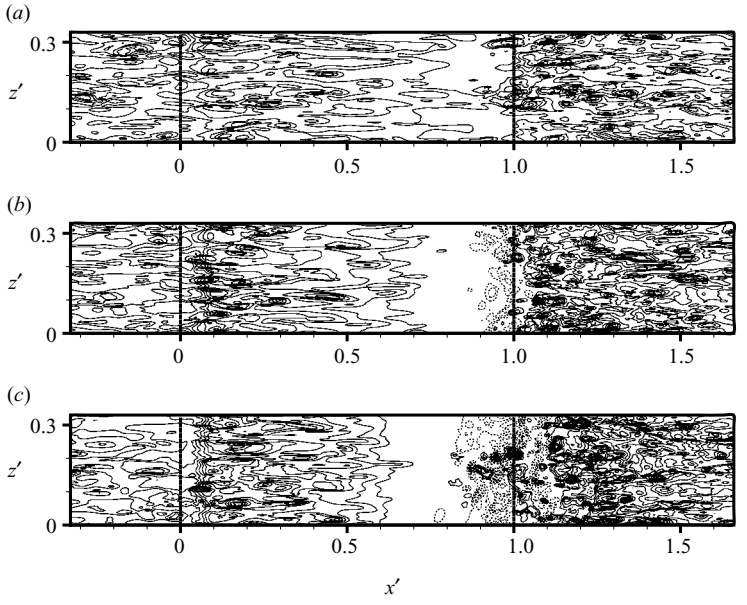

FIGURE 7. Top view of instantaneous skin friction coefficient in the (x, z)-plane. (*a*) $\delta/R = 0.015$, Case 1; (*b*) $\delta/R = 0.030$, Case 2; (*c*) $\delta/R = 0.045$, Case 3.

by integrating $\Phi(k_z, \omega; x)$ over k_z. Each spectrum presented in this paper is normalized such that its integral is equal to the mean-square of the wall pressure fluctuations.

The spectra normalized by the outer variables are illustrated in figure 8. For $\delta/R = 0.015$ (figure 8*a*), the spectra converge in the high-frequency region. For $0.4 < \omega\theta_0/U_\infty$, the spectra decrease with a slope of about -5. The computed spectra decay faster than a -3 slope which is observed experimentally by Simpson, Ghodbane & McGrath (1987). This might be partially due to the low Reynolds number and partially due to the effects of the second-order finite-difference spatial discretization used in the present study (Na & Moin 1998). The pressure spectra shows a negligible region with a slope of -1, which arises from the contribution of motions in the logarithmic region. Since the Reynolds number considered in the present study is relatively low, the logarithmic region is not well defined. The frequency spectra for $\delta/R = 0.030$ and 0.045 are presented in figures 8(*b*) and 8(*c*), respectively. Any spectra scaled for the present turbulent boundary layer over a bump do not converge in the presence of a pressure gradient. This is because that the dynamic pressure is no longer an important parameter in boundary layers with a pressure gradient.

The spatial characteristics of the wall pressure fluctuations are obtained from the two-point correlations as a function of the streamwise spatial (Δx) and temporal (Δt) separations,

$$R_{pp}(\Delta x, \Delta t; x) = \frac{\langle p_w(x, z, t) p_w(x + \Delta x, z, t + \Delta t)\rangle}{(p_w)_{rms}(x, z, t)(p_w)_{rms}(x + \Delta x, z, t + \Delta t)}, \tag{17}$$

where the angle brackets indicate an average over the spanwise direction and time. Again, the dependence on the streamwise location x is considered to be due to the flow inhomogeneity. Contour maps of the two-point correlation for all cases at two streamwise locations are presented in figure 9, where the contour levels are from 0.1 to 0.9 in increments of 0.1. To facilitate comparison, the spatial separations are

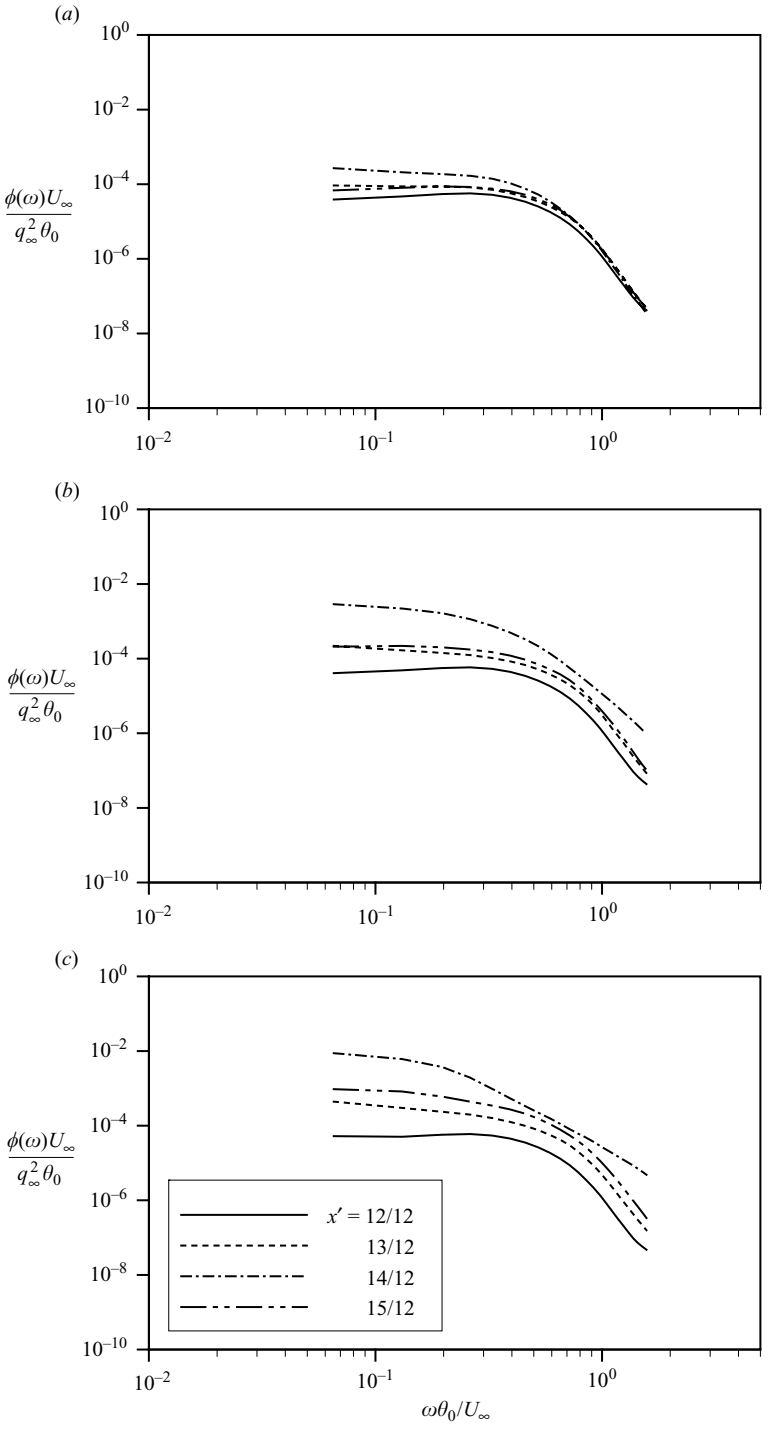

FIGURE 8. Frequency spectra of wall pressure fluctuations with outer variable scaling: (*a*) $\delta/R = 0.015$; (*b*) $\delta/R = 0.030$; (*c*) $\delta/R = 0.045$.

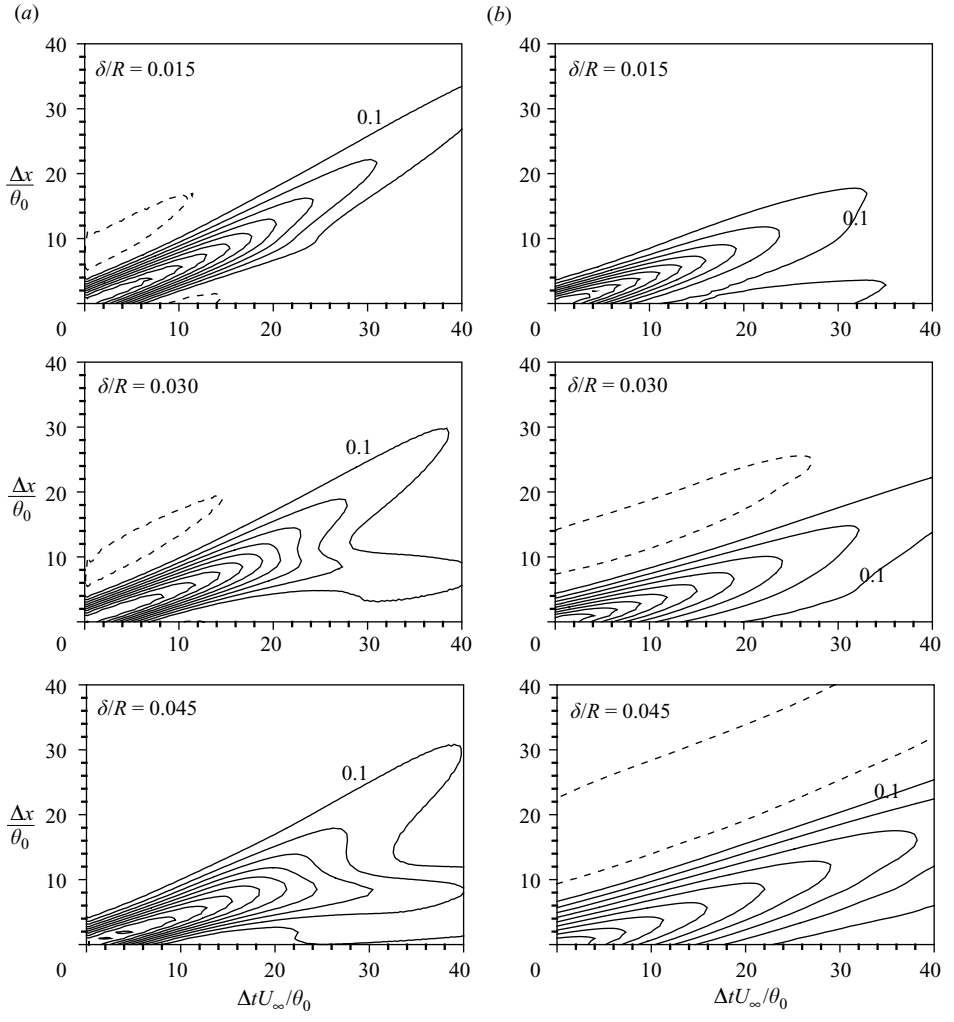

FIGURE 9. Two-point correlation coefficient of wall pressure fluctuations as a function of streamwise spatial and temporal separations: (*a*) $x' = 0$, leading edge; (*b*) $x' = 12/12$, trailing edge.

normalized by the inlet momentum thickness. The strong convective nature of the wall pressure fluctuations is reflected in the concentration of the contours into a band. The convection velocity is denoted by the slope $\Delta x/\Delta t$. The convection velocity of large eddies is higher than that of small eddies, as indicated by a slightly higher value of the slope $\Delta x/\Delta t$. Figure 9 shows that the wall pressure field loses coherence as convection proceeds and as surface curvature increases. Note that the contour plot shows a slightly tilted shape at $x' = 12/12$, indicating that the wall pressure fluctuations do not proceed further downstream.

Figure 10 shows the two-point correlation of the wall pressure fluctuations as a function of the spanwise spatial and temporal separations,

$$R_{pp}(\Delta z, \Delta t; x) = \frac{\langle p_w(x, z, t) p_w(x, z + \Delta z, t + \Delta t)\rangle}{(p_w)_{rms}(x, z, t)(p_w)_{rms}(x, z + \Delta z, t + \Delta t)}, \tag{18}$$

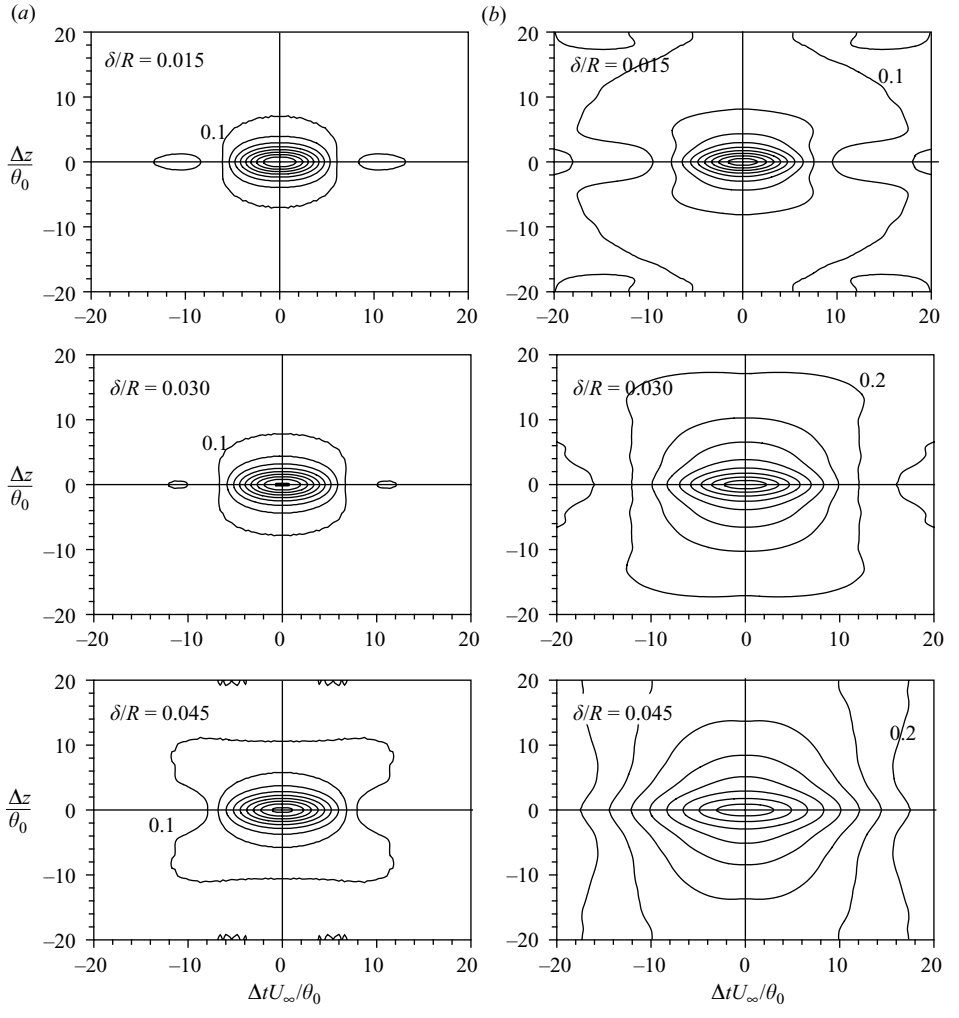

FIGURE 10. Two-point correlation coefficient of wall pressure fluctuations as a function of spanwise spatial and temporal separations: (*a*) $x' = 0$, leading edge; (*b*) $x' = 12/12$, trailing edge.

Here, the brackets indicate an average over the spanwise direction and time. The contour levels are from 0.1 to 0.9 in increments of 0.1. Compared to the contours at $x' = 0$, the contours near the trailing edge of the bump are elongated along the spanwise direction and are more separated for all cases. The spanwise extent of the widest contour (contour level 0.1) increases up to $x' = 12/12$, at which $(p_w)_{rms}$ has a maximum value. This indicates that the spanwise integral length scale of the wall pressure fluctuations increases. The results obtained by examining the correlation coefficients thus reveal a two-dimensional structure of wall pressure fluctuations near the trailing edge of the bump.

4.2. *Flow noise source and far-field noise*

Lighthill's equation for acoustic density fluctuations can be rewritten as,

$$\frac{\partial^2 \rho}{\partial t^2} + \frac{1}{M^2} \frac{\partial^2 \rho}{\partial x_i \partial x_j} = S, \tag{19}$$

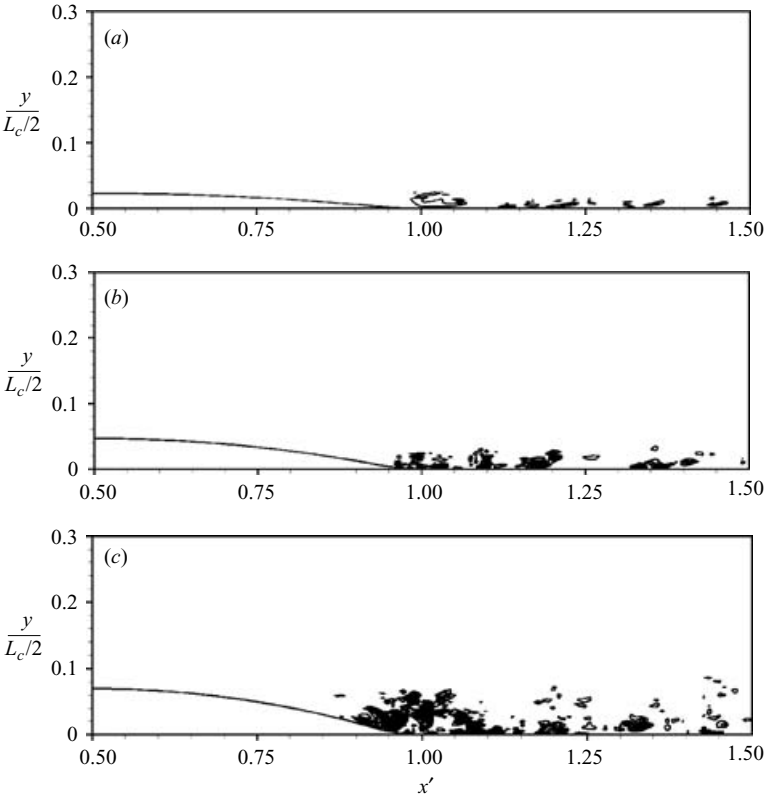

FIGURE 11. Distribution of instantaneous acoustic source in the (x, y)-plane: (*a*) $\delta/R = 0.015$; (*b*) $\delta/R = 0.030$; (*c*) $\delta/R = 0.045$.

where

$$S = \frac{\partial^2}{\partial x_i \partial x_j}\{\rho u_i' u_j' + \delta_{ij}(p - \rho/M^2) - \tau_{ij}\}, \tag{20}$$

is the nominal acoustic source. The acoustic source is small near the leading edge of the bump, which is not shown here. Contour maps of the instantaneous acoustic source near the trailing edge of the bump are shown in figure 11. It is seen that large acoustic sources are located near the trailing edge of the bump, where the streamwise pressure gradient is strongly adverse. The source term S becomes small again by $x' = 1.5$. The strength of the acoustic source increases with increasing the radius of surface curvature δ/R.

Contour maps of the r.m.s. acoustic source calculated using (20) are shown in figure 12. Similar to the behaviour of the instantaneous acoustic source (figure 11), the r.m.s. acoustic source S is small near the leading edge of the bump and bump apex, and reaches a maximum near the trailing edge of the bump. Comparison of figures 12 and 5(*b*) indicates that the location of the dominant acoustic source qualitatively coincides with the location where the wall pressure fluctuations are greatest. This suggests that wall pressure fluctuations are closely correlated with acoustic sources. Such a correlation between acoustic sources and wall pressure fluctuations would call into question the validity of eliminating the dipole source term coming from wall pressure fluctuations in the acoustic source of Lighthill's equations (Powell 1960). A

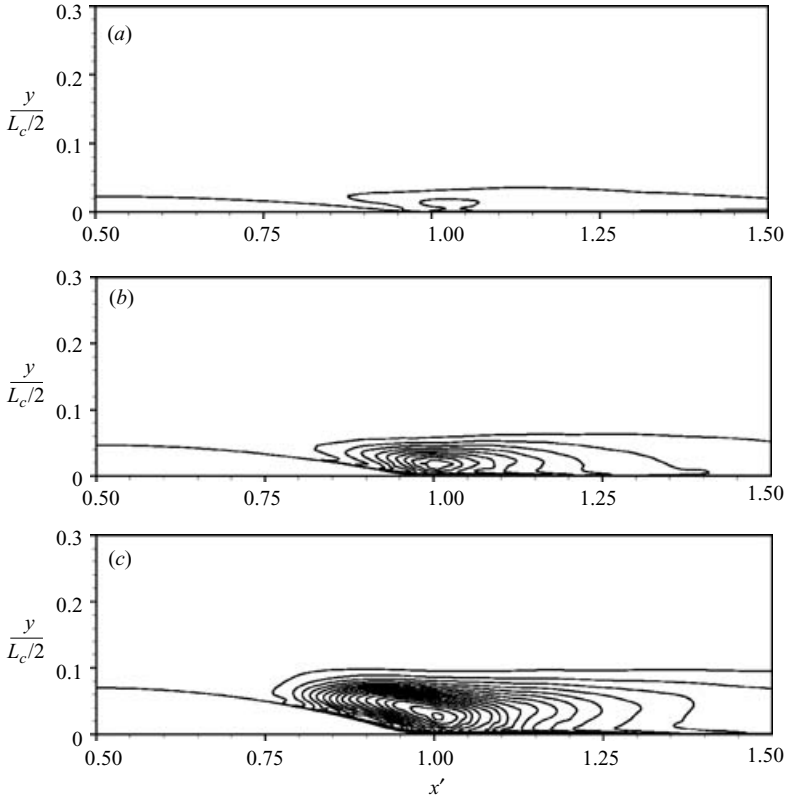

FIGURE 12. Contours of r.m.s. acoustic source in the (x, y)-plane: (a) $\delta/R = 0.015$; (b) $\delta/R = 0.030$; (c) $\delta/R = 0.045$.

more quantitative description of the relationship between wall pressure fluctuations and acoustic sources is presented in figure 14.

To obtain further insight into the acoustic source S, profiles of the acoustic source were examined (figure 13a). For the boundary layer over a flat plate ($\delta/R = 0$), S has the largest r.m.s. value near $y^+ = 20$, which corresponds to the average location of the centre of the streamwise vortices near the wall. Note that for $\delta/R = 0.030$, S is maximum in the viscous sublayer near $y^+ = 5$; this maximum in S is probably related to the generation of the internal layer, which is known to be triggered at discontinuities in the surface curvature (Baskaran *et al.* 1987; Webster *et al.* 1996). A closer inspection of figure 13(b) discloses that the large terms in the viscous sublayer for $\delta/R = 0.030$ are S_{22} and S_{33}, owing to the high turbulence intensities in the wall-normal and spanwise directions, respectively. In sum, the internal layer with strong adverse pressure gradient that forms as a result of the discontinuity in the surface curvature is responsible for the increased acoustic source generation observed near the trailing edge of the bump.

A quantitative statistical description of the relationship between wall pressure fluctuations p_w and acoustic source S is obtained from the correlation $R_{pS}(\Delta x, \Delta y, \Delta z)$ and its corresponding coefficient $R'_{pS}(\Delta x, \Delta y, \Delta z)$, which are defined as

$$R_{pS}(\Delta x, \Delta y, \Delta z) = \langle p(x_0, 0, z, t) S(x_0 + \Delta x, \Delta y, z + \Delta z, t) \rangle, \tag{21}$$

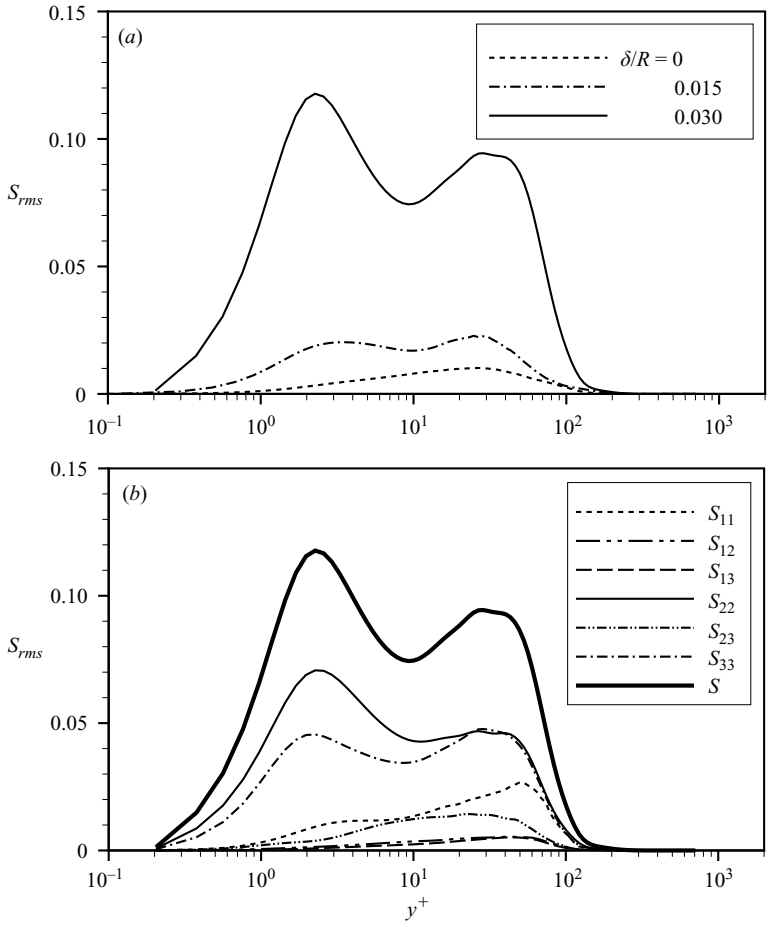

FIGURE 13. Profile of r.m.s. acoustic source at $x' = 1.0$. (*a*) Total source; (*b*) $\delta/R = 0.030$.

and

$$R'_{pS}(\Delta x, \Delta y, \Delta z) = \frac{R_{pS}(\Delta x, \Delta y, \Delta z)}{p_{rms} S_{rms}}, \tag{22}$$

respectively. The angle brackets denote an average over the spanwise direction and time. Using the DNS database for a flat plate turbulent boundary layer (Kim *et al.* 2002), the correlation and its corresponding coefficient are obtained at the centre of the computational domain in a turbulent boundary layer with zero pressure gradient. A typical isosurface of the large magnitude of $R'_{pS}(\Delta x, \Delta y, \Delta z)$ is shown in figure 14. The values of 0.1, approximately 50 % of the maximum magnitude, have been chosen arbitrarily to define the iso-surfaces. Figure 14 exhibits highly correlated acoustic sources upstream of the location at which the wall pressure fluctuations are obtained.

The contour lines of $R'_{pS}(\Delta x, \Delta y, \Delta z)$ in the $(y, z), (x, z)$ and (x, y)-planes are shown in figure 15. The contour levels span from -0.2 to 0.2 in increments of 0.02, and negative correlations are indicated by dashed contours. In the contour map in the (y, z)-plane (figure 15*a*), the maximum correlation coefficient occurs directly above the location of maximum wall pressure fluctuations. Note that no spanwise

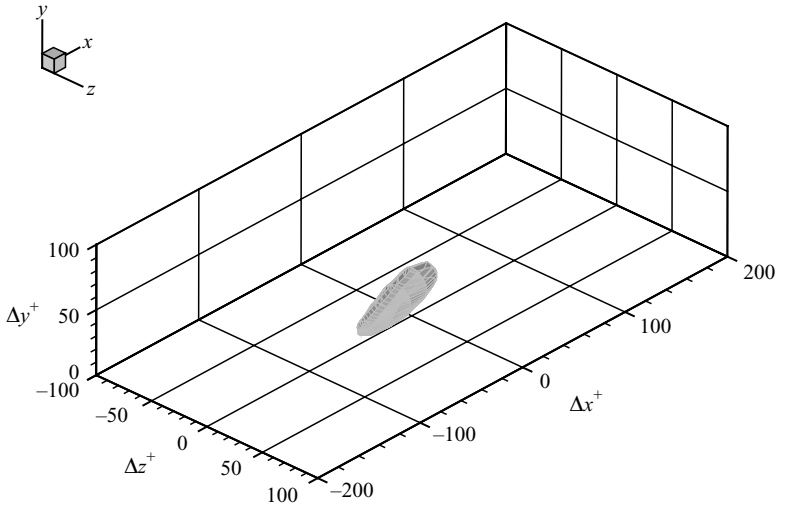

FIGURE 14. Iso-surfaces of correlation coefficient between wall pressure fluctuations and acoustic source.

displacement is observed at $\Delta y^+ = 20$ (figure 15*b*), indicating that the strongest correlation coefficients in the vicinity of the wall are observed directly above the locations of the maximum wall pressure fluctuations. Figure 15(*c*) shows that the location of the maximum correlation coefficient moves away from the wall with increasing Δx^+. This confirms the existence of a tilted structure in the vicinity of the wall. It is seen that the y^+ location of the maximum correlation coefficient increases from $y^+ = 15$ at $\Delta x^+ = -50$ to $y^+ = 20$ at $\Delta x^+ = -10$, which gives a tilt angle of about 7.13°. There is a correlation between wall pressure fluctuations and streamwise vortices (Kim *et al.* 2002). Owing to this relationship, the y^+ location of the maximum correlation coefficient gives a tilt angle.

Figures 16–19 show contours of the far-field acoustic density fluctuations for $\delta/R = 0.0$, 0.015, 0.030 and 0.045, respectively. The contour levels range from -5×10^{-11} to 5×10^{-11} in increments of 2.5×10^{-12}, and contours of negative values are dashed. It is worth pointing out that the extremely small contour levels result from the M^4 and M^3 factors in (10). In the present calculation, based on the acoustic analogy, sufficient arithmetic precision is maintained since the far-field and near-field acoustic densities are evaluated separately. The volume quadrupole contribution to the total acoustic density propagation is $O(M^4)$, whereas the surface dipole contribution is $O(M^3)$. Thus, the effect of the quadrupole source on the far-field acoustic density fluctuations is smaller than that of the dipole source at low Mach numbers. For $\delta/R = 0.0$, it is clearly shown in figure 16 that the total acoustic field has dipole-like characteristics.

The contribution of the volume quadrupoles to the total acoustic field gradually increases with increasing δ/R. The role of the volume quadrupole for $\delta/R = 0.030$ (figure 18) is more important than that for $\delta/R = 0.015$ (figure 17). As can be clearly seen in figure 19, the contribution of the volume quadrupole for $\delta/R = 0.045$ is much larger than the contributions for other cases. We can conclude from the acoustic field results that the total acoustic field shows dipolar characteristics for $\delta/R = 0.0$, 0.015 and 0.030 (figures 16–18), whereas quadrupolar characteristics appear in the

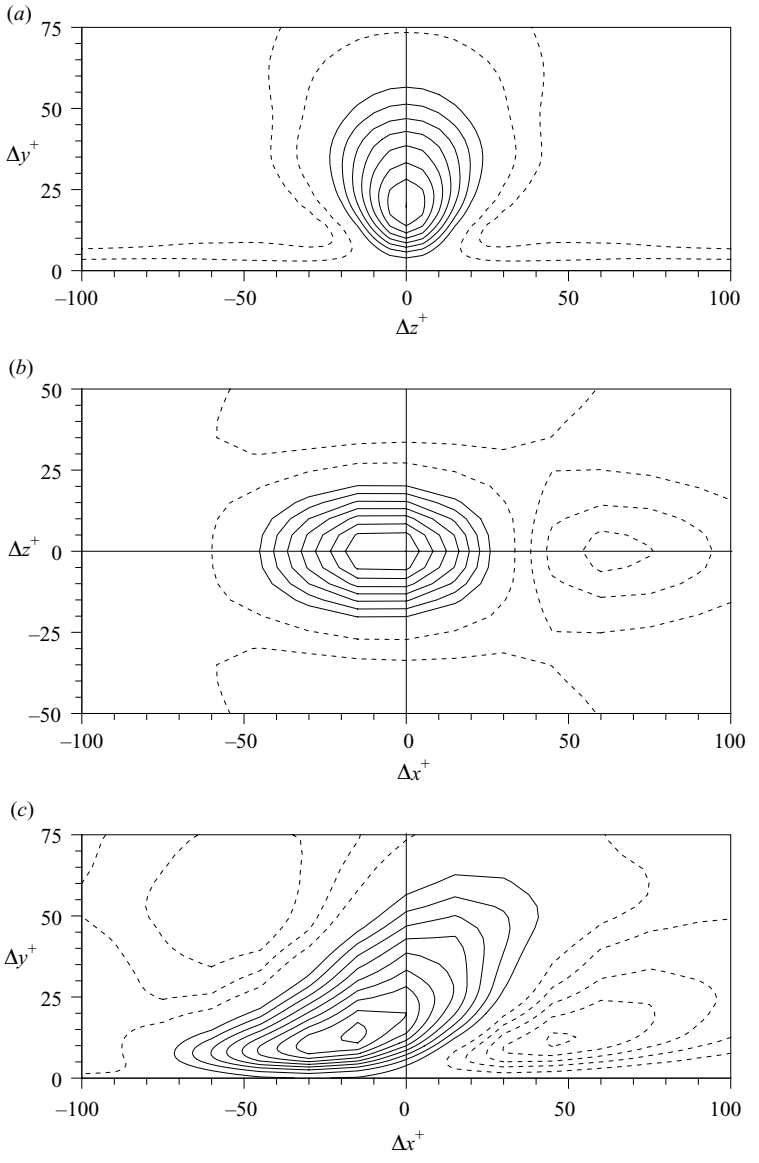

FIGURE 15. Contours of R_{pS}: (*a*) at $\Delta x^+ = 0$ in the (y, z)-plane; (*b*) at $\Delta y^+ = 20$ in the (x, z)-plane; (*c*) at $\Delta z^+ = 0$ in the (x, y)-plane.

total acoustic field for $\delta/R = 0.045$ (figure 19). Therefore, the contribution of the quadrupole source increases with increasing δ/R.

5. Conclusions

A detailed numerical analysis of flow past a surface bump has been performed to scrutinize the effects of longitudinal surface curvature on wall pressure fluctuations and flow-induced noise. Statistical descriptions of the wall pressure fluctuations were obtained by performing DNSs of a turbulent boundary layer over a bump. The skin friction coefficient C_f decreases when the boundary layer is subjected to an adverse

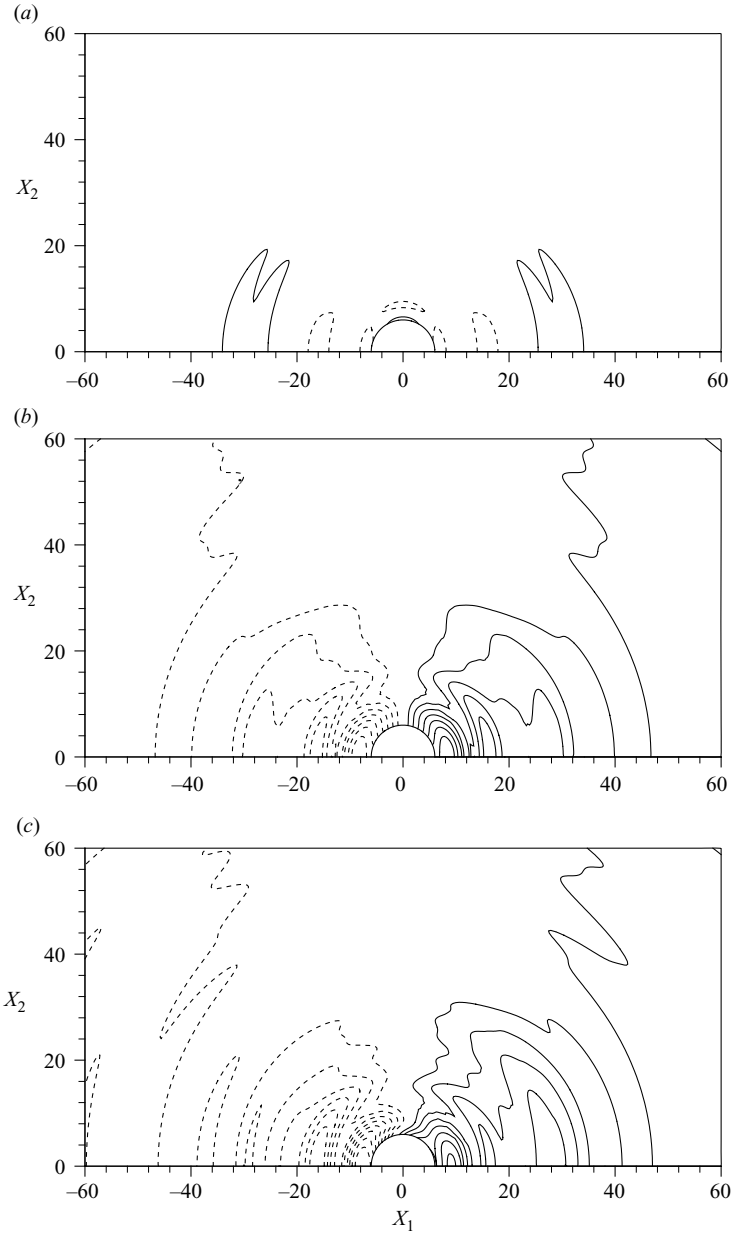

FIGURE 16. Contours of acoustic density fluctuations at $M = 0.01$ for $\delta/R = 0.0$: (*a*) quadrupole; (*b*) dipole; (*c*) total.

pressure gradient, but increases under favourable pressure gradients. Wall pressure fluctuations are significantly enhanced near the trailing edge of the bump, where the boundary layer is subjected to a strong adverse pressure gradient. Large-scale structures in the distribution of wall pressure fluctuations were observed to grow rapidly near the trailing edge of the bump and convect downstream. The spanwise integral length scale of wall pressure fluctuations increases near the trailing edge of the bump. Acoustic sources of the Lighthill equations S near the leading edge are

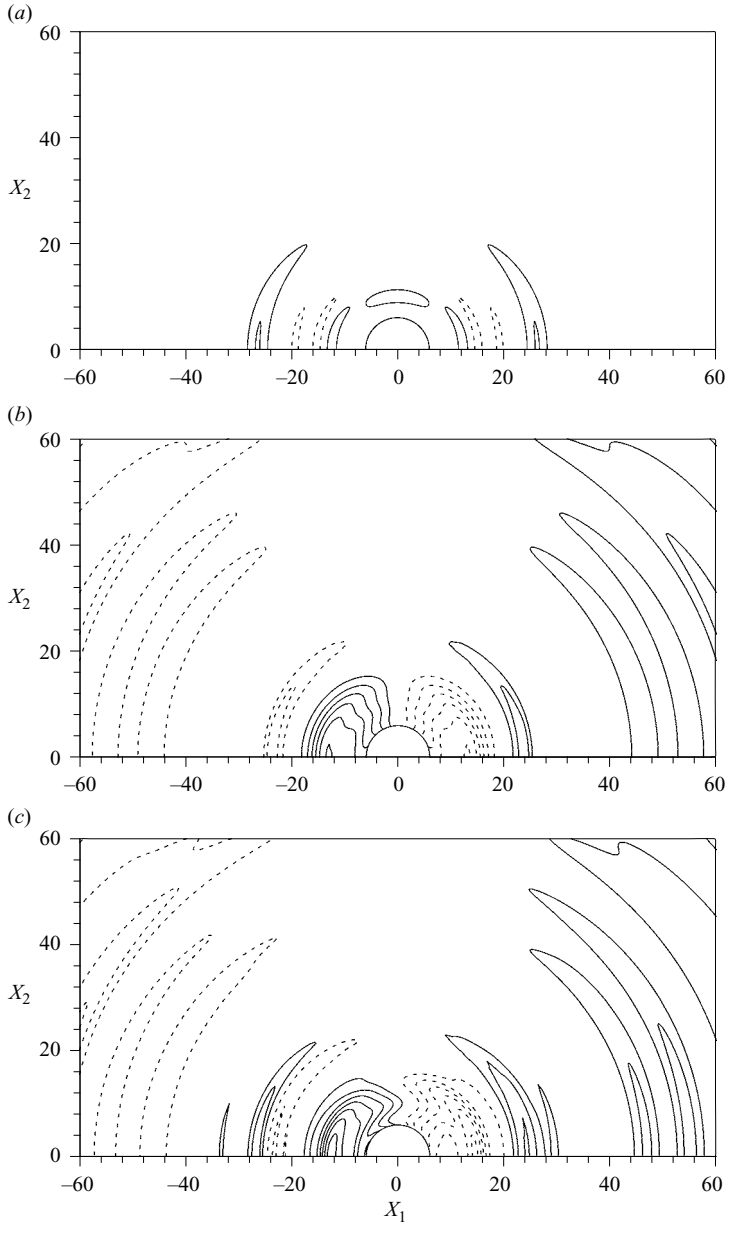

FIGURE 17. Contours of acoustic density fluctuations at $M = 0.01$ for $\delta/R = 0.015$: (*a*) quadrupole; (*b*) dipole; (*c*) total.

smaller than those near the trailing edge of the bump. Large acoustic sources are located near the trailing edge of the bump, where the streamwise pressure gradient is strongly adverse. The strength of the acoustic source increases with increasing radius of surface curvature δ/R. The internal layer triggered by the discontinuity in surface curvature near the trailing edge of the bump is responsible for increased acoustic source generation in this region. The strongest correlations between p_w and S in the vicinity of the wall are observed directly above the locations of maximum wall

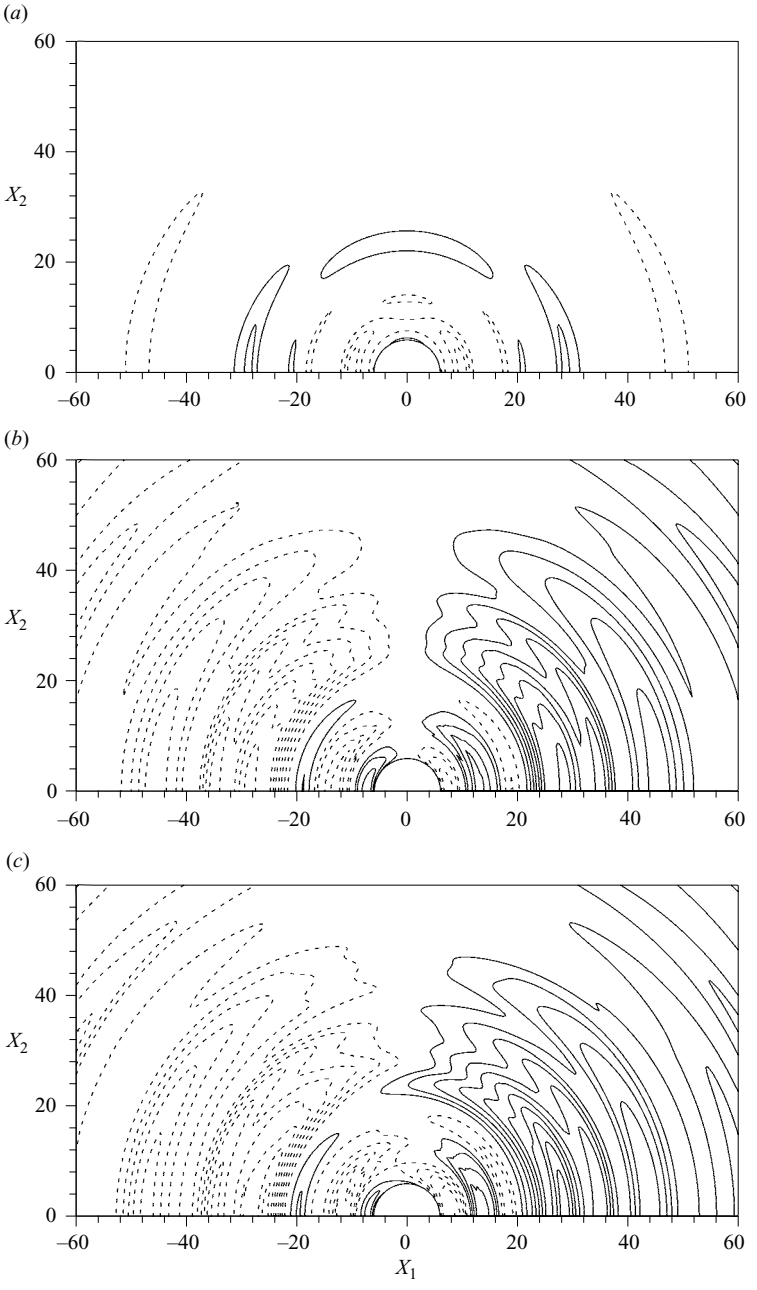

FIGURE 18. Contours of acoustic density fluctuations at $M = 0.01$ for $\delta/R = 0.030$: (*a*) quadrupole; (*b*) dipole; (*c*) total.

pressure fluctuations. Such a correlation between acoustic sources and wall pressure fluctuations would call into question the validity of eliminating the dipole source term coming from wall pressure fluctuations in the acoustic source of Lighthill's equations. The effect of the quadrupole source on the far-field acoustic density fluctuations is smaller than that of the dipole source. The contribution of the volume quadrupoles

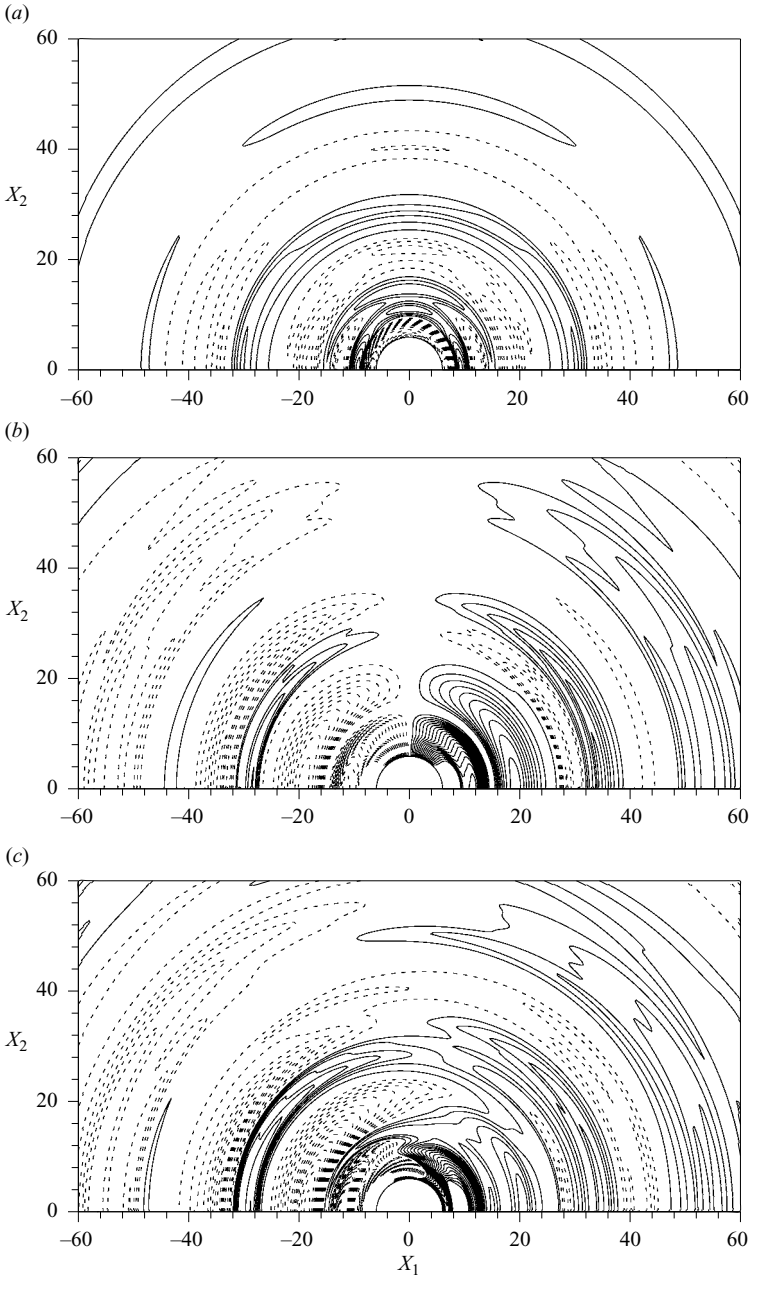

FIGURE 19. Contours of acoustic density fluctuations at $M = 0.01$ for $\delta/R = 0.045$: (*a*) quadrupole; (*b*) dipole; (*c*) total.

to the total acoustic field gradually increases with increasing radius of the surface curvature δ/R.

The authors would like to acknowledge the support from KISTI (Korea Institute of Science and Technology Information) under 'The Sixth Strategic Supercomputing

Support Program'. The use of the computing system of the Supercomputing Center is also greatly appreciated.

REFERENCES

Baskaran, V., Smits, A. J. & Joubert, P. N. 1987 A turbulent flow over a curved hill. Part 1. Growth of an internal boundary layer. *J. Fluid Mech.* **182**, 47–83.

Bradshaw, P. 1973 Effects of streamline curvature on turbulent flow. *AGARDograph* **169**.

Choi, H. & Moin, P. 1990 On the space–time characteristics of wall-pressure fluctuations. *Phys. Fluids* A**2**, 1450–1460.

Choi, H. & Moin, P. 1994 Effects of the computational time step on numerical solutions of turbulent flow. *J. Comput. Phys.* **113**, 1–4.

Choi, H., Moin, P. & Kim, J. 1993 Direct numerical simulation of turbulent flow over riblets. *J. Fluid Mech.* **255**, 503–539.

Curle, N. 1955 The influence of solid boundaries upon aerodynamic sound. *Proc. R. Soc. Lond.* A **231**, 505–514.

Kim, J. 1989 On the structure of pressure fluctuations in simulated turbulent channel flow. *J. Fluid Mech.* **205**, 421–451.

Kim, J., Choi, J.-I. & Sung, H. J. 2002 Relationship between wall pressure fluctuations and streamwise vortices in a turbulent boundary layer. *Phys. Fluids* **14**, 898–901.

Kim, J., Kim, K. & Sung, H. J. 2003 Wall pressure fluctuations in a turbulent boundary layer after blowing or suction. *AIAA J.* **41**, 1697–1704.

Landahl, M. T. 1975 Wave mechanics of boundary layer turbulence and noise. *J. Acoust Soc. Am.* **57**, 824–831.

Lighthill, M. J. 1952 On sound generated aerodynamically: I. General theory. *Proc. R. Soc. Lond.* A **211**, 564–587.

Lund, T. S., Wu, X. & Squires, K. D. 1998 Generation of turbulent inflow data for spatially-developing boundary layer simulations. *J. Comput. Phys.* **140**, 233–258.

Na, Y. & Moin, P. 1998 The structure of wall-pressure fluctuations in turbulent boundary layers with adverse pressure gradient and separation. *J. Fluid Mech.* **77**, 347–373.

Neves, J. C. & Moin, P. 1994 Effects of convex transverse curvature on wall-bounded turbulence. Part 2. The pressure fluctuations. *J. Fluid Mech.* **272**, 383–406.

Patel, V. C. 1965 Calibration of the Preston tube and limitations on its use in adverse pressure gradients. *J. Fluid Mech.* **23**, 185–208.

Powell, A. 1960 Aerodynamic noise and the plane boundary. *J. Acoust Soc. Am.* **32**, 982–990.

Simpson, R. L., Ghodbane, M. & McGrath, B. E. 1987 Surface pressure fluctuations in a separating turbulent boundary layer. *J. Fluid Mech.* **177**, 167–186.

Spalart, P. R. 1988 Direct simulation of a turbulent boundary layer up to $Re_\theta = 1410$. *J. Fluid Mech.* **187**, 61–98.

Thomas, P. D. & Middlecoff, J. F. 1980 Direct control of the grid point distribution in meshes generated by elliptic equations. *AIAA J.* **18**, 652–656.

Wang, M., Lele, S. K. & Moin, P. 1996 Computation of quadrupole noise using acoustic analogy. *AIAA J.* **34**, 2247–2254.

Webster, D. R., DeGraaff, D. B. & Eaton, J. K. 1996 Turbulence characteristics of a boundary layer over a two-dimensional bump. *J. Fluid Mech.* **320**, 53–69.

Wu, X. & Squires, K. D. 1998 Numerical investigation of the turbulent boundary layer over a bump. *J. Fluid Mech.* **362**, 229–271.